

A numerical study of particle wall-deposition in a turbulent square duct flow

C.M. Winkler^{a,*}, Sarma L. Rani^b, S.P. Vanka^c

^a *The Boeing Company, P.O. Box 516, St. Louis, MO 63166, USA*

^b *CFD Research Corporation, 215 Wynn Drive, Huntsville, AL 35805, USA*

^c *Department of Mechanical and Industrial Engineering, 1206 W. Green Street, University of Illinois at Urbana-Champaign, Urbana, IL 61801, USA*

Received 16 August 2005; received in revised form 8 August 2006; accepted 22 August 2006

Available online 30 August 2006

Abstract

The deposition of dense solid particles in a downward, fully developed turbulent square duct flow at $Re_\tau=360$, based on the mean friction velocity and the duct width, is studied using large eddy simulations of the fluid flow. The fluid and the particulate phases are treated using Eulerian and Lagrangian approaches, respectively. A finite-volume based, second-order accurate fractional step scheme is used to integrate the incompressible form of the unsteady, three-dimensional, filtered Navier–Stokes equations on an $80 \times 80 \times 128$ grid. A dynamic subgrid kinetic energy model is used to account for the unresolved scales. The Lagrangian particle equation of motion includes the drag, lift, and gravity forces and is integrated using the fourth-order accurate Runge–Kutta scheme. Two values of particle to fluid density ratio ($\rho_p/\rho_f=1000$ and 8900) and five values of dimensionless particle diameter ($d_p/\delta \times 10^6=100, 250, 500, 1000$ and 2000, δ is the duct width) are studied. Two particle number densities, consisting of 10^5 and 1.5×10^6 particles initially in the domain, are examined.

Variations in the probability distribution function (PDF) of the particle deposition location with dimensionless particle response time, i.e. Stokes number, are presented. The deposition is seen to occur with greater probability near the center of the duct walls, than at the corners. The average streamwise and wall-normal deposition velocities of the particles increase with Stokes number, with their maxima occurring near the center of the duct wall. The computed deposition rates are compared to previously reported results for a circular pipe flow. It is observed that the deposition rates in a square duct are greater than those in a pipe flow, especially for the low Stokes number particles. Also, wall-deposition of the low Stokes number particles increases significantly by including the subgrid velocity fluctuations in computing the fluid forces on the particles. Two-way coupling and, to a greater extent, four-way coupling are seen to increase the deposition rates.

© 2006 Elsevier B.V. All rights reserved.

Keywords: Large eddy simulation; Gas–particle flow; Particle deposition

1. Introduction

Recently, we have examined the preferential concentration of particles in a fully developed turbulent square duct flow [1]. This work shows that particles preferentially accumulate in selective regions of the duct, depending on their Stokes number. The current work extends the above study by evaluating the characteristics of particle wall-deposition in a square duct. It is well known that the instantaneous turbulent flow structures lead to preferential concentration of particles into selective regions of the flow and thereby, influence their deposition characteristics [2–4]. A good understanding of the particle deposition phenomenon can lead to improved designs of several engineering

equipment, such as powder coating devices and ducting for clean-room applications. Due to the ease with which computational fluid dynamics (CFD) allows calculation of quantities that are often difficult to measure through experiments, it has become a valuable tool to study gas–particle flows.

Computational approaches for predicting particle-laden turbulent flows can generally be classified as either Eulerian–Eulerian or Eulerian–Lagrangian. In the Eulerian–Eulerian method, the carrier and the dispersed phases are both treated as continua, and equations governing their mass and momentum transport are derived and solved. In such an approach, particle–particle interactions are modeled as additional diffusive terms. Typically, the Eulerian–Eulerian method, also known as the two-fluid method, is more appropriate for flows with high volume fractions of the dispersed phase. In the Eulerian–Lagrangian method, individual particle trajectories are computed by solving

* Corresponding author.

E-mail address: chad.m.winkler@boeing.com (C.M. Winkler).

Nomenclature

A	Area of deposition
C_d	Drag coefficient
d_p	Particle diameter
f	Particle feedback force
g	Gravitational force
k_{sgs}	Subgrid kinetic energy
m	Mass
N	Number of particles at beginning of sampling time
N_d	Number of deposited particles
N_i	Number of initial particles
p	Pressure
Re_τ	Friction Reynolds number
t	Time
u	Velocity in x direction (cross-sectional velocity)
u_τ	Friction velocity
v	Velocity in y direction (cross-sectional velocity)
V	Volume of domain
V_d	Deposition rate
w	Velocity in z direction (streamwise velocity)
x	Spanwise coordinate
y	Spanwise coordinate
z	Streamwise coordinate
x_i	Coordinate direction (index notation)

Greek symbol

δ	Duct width
ε	Dissipation rate
ϕ_v	Particle volume fraction
ν	Kinematic viscosity
ν_T	Eddy viscosity
ρ	Density
τ_p^+	Particle response time (wall units)
τ_p	Particle response time
$\tilde{\tau}_p$	Particle response time (outer units)
τ_w	Wall shear stress

Subscripts

p	particle
f	fluid

the Lagrangian particle equations of motion, while the carrier gas phase is treated using the Eulerian approach. However, due to the computational cost of tracking a large number of individual particles, Lagrangian methods typically are appropriate for flows with low volume fractions of the dispersed phase. A recent summary of computational methods for particle-laden flows is given by Loth [5].

The numerical schemes for the carrier phase can be classified further according to the degree of resolution of the turbulent flow scales. Direct Numerical Simulation (DNS) is the most accurate method for simulating turbulence. In DNS, all scales of motion are resolved without any empiricism. The only errors

that arise in DNS are from the numerical method used to solve the equations of motion. Due to the large computational resources needed to resolve all scales of motion, DNS is currently limited to relatively low Reynolds number flows. On the other hand, large eddy simulations (LES) resolve only the large, energy containing scales in the flow and model the effects of the small scales. Modeling of the unresolved, or subgrid, scales has brought about several approaches for LES of single phase flows. A recent review of such LES techniques is given in Meneveau and Katz [6].

Large eddy simulations of turbulent, particle-laden flows have also been pursued with inclusion of one-way and two-way

coupling between the phases. In one-way coupling, the particles are transported by the surrounding fluid, but are assumed not to impact the fluid flow in turn. In two-way coupling, the particle feedback effects on the fluid are also included. A number of studies on particle deposition in geometries with two homogeneous directions such as channels and circular pipes have been reported [7–11]. Particle deposition in a channel flow was studied by Wang and Squires [7]. They used the dynamic Smagorinsky model in conjunction with a one-way coupling approach. Reynolds numbers of 180 and 1000, based on channel half-width and friction velocity, were examined. They assumed that particle deposition occurred whenever a particle was within a distance of one radius from the wall. Initially, particle velocities were equal to the local fluid velocity and 20,000 particles per particle response time were randomly placed in the channel. A lift force due to fluid shear was also included, but was seen to be small in comparison to the drag. The streamwise velocity slip ratio was found to be larger than the wall normal slip ratio. The maximum particle concentration was found to be near the wall. The comparison between the LES and DNS results was better for particles having the largest relaxation times. This is because larger particles are less likely to be influenced by the small scales which are modeled, rather than computed, in LES. When a subgrid kinetic energy model was used to include the effects of subgrid fluctuation velocity in the particle equation of motion, they found that there was no significant effect on large particles. On the other hand, for small particles, the wall-normal component of the average deposition velocity was increased by as much as 30%. It was also found that inclusion of the lift force increases particle deposition.

Zhang and Ahmadi [8] examined aerosol particle transport and deposition in a channel. A $16 \times 64 \times 64$ spectral grid without a subgrid model was used in the simulations. Their particle equation of motion included lift, drag, gravity, and Brownian diffusion. A total of 8192 particles were used in their simulations to evaluate statistics. For horizontal ducts, they found that gravity increases deposition by sedimentation on the lower wall. For vertical ducts with gravity in the flow direction, deposition rates were higher since the lift force is directed towards the walls if the particles are large, i.e. have settling velocities at least on the order of the fluid velocity. Brownian diffusion was shown only to be important for particles smaller than $0.1 \mu\text{m}$.

Uijtewaal and Oliemans [9] examined particle dispersion and deposition in vertical pipes of circular cross-section. They used LES at friction Reynolds numbers of 360, 1000, and 2100 to compute particle deposition for relaxation times τ_p^+ (in wall units; see Section 2.3 for definition) ranging from 5 to 10^4 . They found that the deposition coefficient scales with the turbulence integral time scale. The wall impact velocity was seen to peak around $\tau_p^+ = 200$. They also observed that the subgrid turbulence has a relatively larger effect on dispersion of smaller particles.

Brooke et al. [10] examined the free-flight mixing and deposition of aerosol particles using DNS of a channel flow. They found that particles deposit in one of two ways: diffusion or free flight towards the wall. The latter was seen to be the dominant mechanism. Free flight of a particle was assumed to begin when the velocities of a particle and the fluid element at

that location are equal. They point out that it is more likely for the particles to be ejected from the near wall layer, and then travel back to the wall in free flight.

DNS of particle deposition in a channel with a free slip surface was examined by van Haarlem et al. [11]. They studied two particle sizes with relaxation times, τ_p^+ , of 5 and 15, and used 200,000 particles for each case. One-way coupling was assumed. For $\tau_p^+ = 5$, deposition rates were higher for the free slip channel than the no-slip channel. But for $\tau_p^+ = 15$, the trend was reversed. For either case, $\tau_p^+ = 15$ had higher deposition rates than $\tau_p^+ = 5$. They find that particles which deposit on the wall were brought by fluid fluctuations which originated far from the wall, confirming the free flight study done by Brooke et al. [10].

Despite the relatively large number of works on particle deposition in turbulent flows, there is a lack of information on this phenomenon in more complex flows such as in a square duct. In the present study, particle deposition in a fully developed turbulent square duct flow is investigated. For single-phase flow, one of the first LES studies of secondary flows in a square duct was performed on a $65 \times 65 \times 32$ grid by Madabhushi and Vanka [12] using the Smagorinsky model. They studied flow at $Re_\tau = 360$, based on duct width and average friction velocity. LES was shown to successfully predict the turbulence driven secondary flows (Fig. 1). They found that the instantaneous velocities in the cross-sectional plane (shown in Fig. 2) can be as high as 10 times their time-averaged values. The secondary flows were shown to convect mean flow momentum from the duct center to its corners, causing a bulging of the streamwise velocity contours towards the corners. Other studies of secondary flows include those by Demuren and Rodi [13], Kajishima and Miyake [14], Gavrilakis [15], Huser and Biringer [16], and Madabhushi and Vanka [17].

In the present effort, we have studied the transport of particles by the turbulence structures in a square duct. Particles

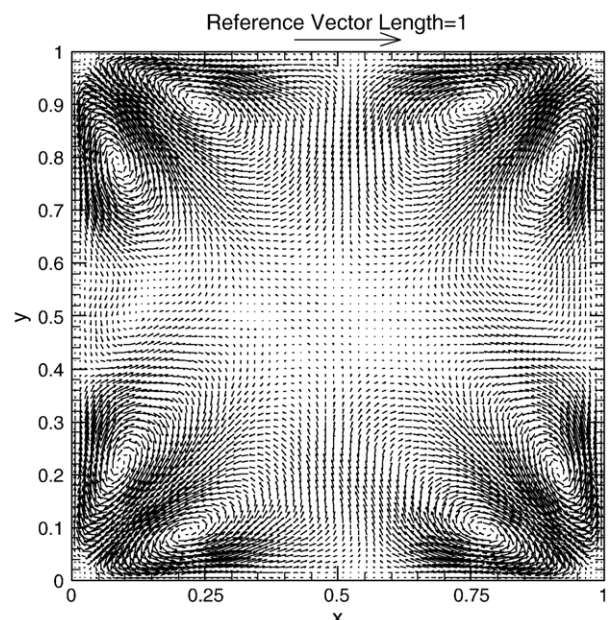


Fig. 1. Mean secondary flows in a square duct.

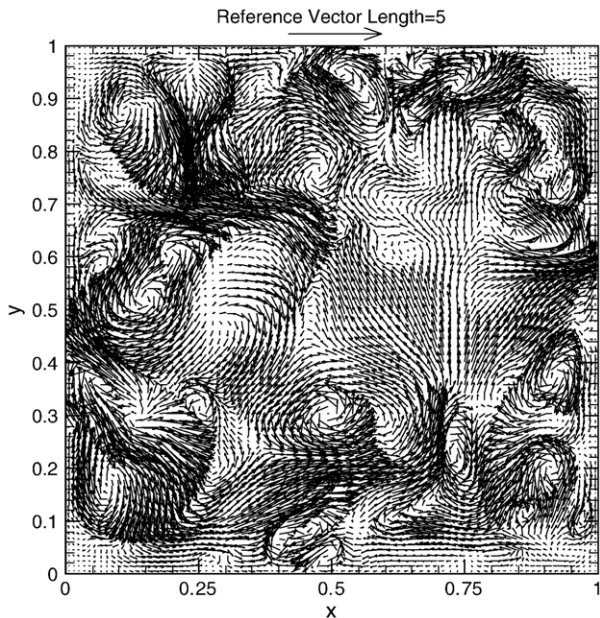


Fig. 2. Instantaneous cross-sectional velocities in a square duct.

with different response times are considered and the rates of their deposition on the duct walls computed. We have also investigated the effects of two-way and four-way interactions between the fluid and the particles on deposition.

2. Details of the simulations

2.1. Numerical method

The incompressible, three-dimensional, unsteady Navier–Stokes equations are given by

$$\nabla \cdot \mathbf{u} = 0 \quad (1)$$

$$\frac{\partial \mathbf{u}}{\partial t} + \nabla \cdot (\mathbf{u}\mathbf{u}) = -\nabla p + \frac{1}{Re_\tau} \nabla^2 \mathbf{u} - \mathbf{f} \quad (2)$$

The components of the velocity vector \mathbf{u} in the two wall-normal and streamwise directions are u , v and w , respectively. The term \mathbf{f} on the right hand side of Eq. (2) represents the sum of the forces exerted by the fluid on the particles (drag and lift) and, accounts for the effects of particles on the carrier phase. This term is zero for one-way coupling simulations.

Top-hat filtering, implemented through finite-volume implicit grid-filtering, was used to generate the equations governing the transport of the large eddies. After filtering, the equations of motion become the following:

$$\nabla \cdot \bar{\mathbf{u}} = 0 \quad (3)$$

$$\begin{aligned} \frac{\partial \bar{u}_i}{\partial t} + \frac{\partial}{\partial x_j} (\bar{u}_i \bar{u}_j) &= -\frac{\partial \bar{P}}{\partial x_i} + \frac{\partial}{\partial x_j} \left[\left(\frac{1}{Re_\tau} + v_T \right) \frac{\partial \bar{u}_i}{\partial x_j} \right] \\ &+ \frac{\partial}{\partial x_j} \left(v_T \frac{\partial \bar{u}_j}{\partial x_i} \right) + 4\delta_{i3} - \bar{f} \end{aligned} \quad (4)$$

The “overbar” notation denotes application of the top-hat filter. The penultimate term on the right hand side of Eq. (4), $4\delta_{i3}$, represents the mean streamwise pressure gradient that balances the total shear force for a fully-developed square duct flow. The filtered pressure gradient term $\partial \bar{P} / \partial x_i$ excludes the mean streamwise pressure gradient but includes the normal (or diagonal) components of the subgrid scale stresses. The eddy viscosity v_T is determined from the subgrid kinetic energy, as will be described shortly in Section 2.2.

The governing Eqs. (3) and (4) are solved using a second-order accurate finite volume method on a collocated grid with central differencing of the spatial derivatives. The velocities have been made dimensionless by the friction velocity, $u_T = (\tau_w / \rho_f)^{1/2}$ and the distances using duct width δ . The characteristic time scale used is δ/u_T . Diffusion and the convective terms are discretized with the Crank–Nicholson and the second-order accurate Adams–Bashforth schemes, respectively. The Harlow–Welch fractional step method was used to decouple the momentum and continuity equations. An algebraic multigrid solver was used to solve the pressure Poisson equation resulting from the fractional step method. The square duct dimensions in the x , y , and z directions are $\delta \times \delta \times 2\pi\delta$ and the grid consisted of 819,200 unstructured Cartesian cells. The friction Reynolds number (Re_τ) based on the mean friction velocity u_T and duct width δ is 360. The dimensionless time step was set to 5×10^{-4} .

Since the particle locations do not necessarily coincide with the fluid velocity grid locations, \bar{f} must be calculated at the fluid velocity positions. In the current simulations, a given particle contributes its feedback (drag and lift) to a finite set of fluid grid points surrounding the particle. The approach first requires the calculation of fluid velocities at the particle position. The interpolation of the fluid velocities to a given particle location, called forward interpolation, is done using second-order accurate Lagrange polynomials involving 27 surrounding fluid grid points. Once \bar{f} at a particle location has been calculated, it is interpolated back to the 27 surrounding grid points where the velocities are located. This “back interpolation” is carried out using the same Lagrange weighting functions that were calculated for forward interpolation. As recommended by Sundaram and Collins [18], the forward and back interpolations were symmetric for accurate numerical representation of the overall (fluid+particle) energy balance equation.

2.2. Subgrid modeling

The unresolved scales are modeled with the dynamic subgrid kinetic energy model developed by Kim and Menon [19]. A test-filter grid, having a resolution of $40 \times 40 \times 64$ in the two wall normal (x and y) and streamwise (z) directions, respectively, was first generated. A 2.5% geometric grid stretching away from all the walls was used in the wall-normal directions. Each test-filter grid cell was then subdivided into eight uniform fine-grid cells, which gave a final grid resolution of $80 \times 80 \times 128$. The first node away from the wall in the finer grid was located at $y^+ = 1.76$ ($y^+ = y/(v/u_T)$). This corresponds to a near wall cell size of $\Delta x^+ = \Delta y^+ = 3.52$. Near the duct center, the cell size was $\Delta x^+ = \Delta y^+ = 5.63$. The streamwise cell size was uniform and

was held fixed at $\Delta z^+ = 17.67$. Note that the lengths in the governing equations are already non-dimensionalized with the duct width δ . Hence, these dimensionless lengths are obtained in the wall units by multiplying them with the frictional Reynolds number Re_τ .

The dynamic subgrid kinetic energy model employed in this work [19] is summarized below. The transport equation for the subgrid kinetic energy, k_{sgs} , is written as

$$\frac{\partial k_{\text{sgs}}}{\partial t} + \bar{u}_i \frac{\partial k_{\text{sgs}}}{\partial x_i} = v_T |\bar{S}|^2 - \varepsilon + \frac{\partial}{\partial x_i} \left(v_T \frac{\partial k_{\text{sgs}}}{\partial x_i} \right) \quad (5)$$

where the eddy viscosity, v_T , is given by

$$v_T = C_t \bar{\Delta} k_{\text{sgs}}^{1/2} \quad (6)$$

and the dissipation rate, ε , is given by

$$\varepsilon = C_e \frac{k_{\text{sgs}}^{3/2}}{\bar{\Delta}} \quad (7)$$

where $\bar{\Delta}$ is the average grid size and C_e and C_t are dynamically determined. The average grid size is here defined as

$$\bar{\Delta} = (\Delta_x \Delta_y \Delta_z)^{1/3} \quad (8)$$

The resolved strain-rate tensor \bar{S} is expressed as

$$\bar{S}_{ij} = \frac{1}{2} \left(\frac{\partial \bar{u}_i}{\partial x_j} + \frac{\partial \bar{u}_j}{\partial x_i} \right) \quad (9)$$

and its magnitude is defined as

$$|\bar{S}| = \sqrt{2 \bar{S}_{ij} \bar{S}_{ij}} \quad (10)$$

The “hat” notation symbolizes the application of the test filter to a quantity and the “overbar” the application of the grid filter. The Leonard stress tensor is then defined as

$$L_{ij} = \widehat{\bar{u}_i \bar{u}_j} - \hat{\bar{u}_i} \hat{\bar{u}_j} \quad (11)$$

The kinetic energy at the test filter level can be found from the trace of Eq. (11)

$$k_{\text{test}} = \frac{1}{2} \left(\widehat{\bar{u}_k \bar{u}_k} - \hat{\bar{u}_k} \hat{\bar{u}_k} \right) \quad (12)$$

The dissipation at the test filter level is expressed as

$$\varepsilon_{\text{test}} = (v + v_T) \left(\frac{\partial \widehat{\bar{u}_i}}{\partial x_j} \frac{\partial \widehat{\bar{u}_i}}{\partial x_j} - \frac{\partial \hat{\bar{u}_i}}{\partial x_j} \frac{\partial \hat{\bar{u}_i}}{\partial x_j} \right) \quad (13)$$

Through a similarity assumption between the subgrid stress tensor and the Leonard stress tensor, one can arrive at the following equation

$$L_{ij} = -2C_t \bar{\Delta} k_{\text{test}}^{1/2} \hat{\bar{S}}_{ij} + \frac{1}{3} \delta_{ij} L_{kk} \quad (14)$$

The least-square method of Lilly [20] is then used to obtain a formula for C_t

$$C_t = \frac{1}{2} \frac{L_{ij} \sigma_{ij}}{\sigma_{ij} \sigma_{ij}} \quad (15)$$

where

$$\sigma_{ij} = -\hat{\bar{A}} k_{\text{test}}^{1/2} \hat{\bar{S}}_{ij} \quad (16)$$

By invoking a similarity assumption between the dissipation at the test filter and grid filter level, an equation for the dissipation at the test filter level is given as

$$\varepsilon_{\text{test}} = C_e \frac{k_{\text{test}}^{3/2}}{\bar{\Delta}} \quad (17)$$

One may now calculate C_t and C_e . These constants have been constrained to be positive in the current simulations. Due to the dynamic evaluation of C_t and C_e , no wall models are needed in the simulations to damp the eddy viscosity. Thus, the traditional Van Driest damping on subgrid viscosity has not been applied.

2.3. Particle motion

The particle equation of motion includes drag and lift in the two wall directions (x and y) and gravity in the streamwise direction (z). The equation is given as:

$$\begin{aligned} m_p \frac{d\mathbf{u}_p}{dt} &= m_p \frac{(\bar{\mathbf{u}}(x_p) - u_p)}{\tau_p} + (m_p - m_f) \mathbf{g} \\ &+ 3.08 m_p \frac{v^{1/2}}{d_p \frac{\rho_p}{\rho_f}} (w - w_p) \left| \frac{\partial w}{\partial x} \right|^{1/2} \text{sgn} \left(\frac{\partial w}{\partial x} \right) \delta_{11} \\ &+ 3.08 m_p \frac{v^{1/2}}{d_p \frac{\rho_p}{\rho_f}} (w - w_p) \left| \frac{\partial w}{\partial y} \right|^{1/2} \text{sgn} \left(\frac{\partial w}{\partial y} \right) \delta_{12} \end{aligned} \quad (18)$$

where \mathbf{u}_p is the particle velocity vector with w_p being its streamwise component, m_p and m_f are the particle mass and the fluid mass displaced by the particle respectively, \mathbf{g} is gravitational acceleration, d_p is the particle diameter, ρ_p and ρ_f are the particle and fluid densities, respectively, and v is the kinematic viscosity. The notation “sgn” implies taking the sign of the bracketed quantity. The lift forces due to secondary flows have been neglected because of the relatively small velocities and gradients in the cross-sectional direction when compared to the corresponding values in the streamwise direction. The lift force is represented by the Saffman expression, which is strictly valid only for small Re_p ($Re_p < 1$). However, the use of the Saffman expression is justified on the basis that the lift force is generally small compared to the drag force even for high inertia particles (when Re_p does not satisfy the above criterion) [7]. This is also confirmed in our recent calculations [21]. A similar observation was made by Loth [5], who noted that for all heavy particles, the lift force makes only a small contribution to the right hand side of Eq. (18). Note that in this study the streamwise flow is oriented in the direction of gravity (downward flow). This

causes lift forces on the particles to be directed towards the walls, in contrast to the case when gravity is opposite to the flow direction. However, since the lift forces are in general small, their relative effect on both downward and upward flows will be small in comparison with the effects of turbulence driven secondary flows.

The particle response time is given as

$$\tau_p = \frac{4d_p\rho_p}{3C_d\rho_f|\bar{\mathbf{u}}(x_p)-\mathbf{u}_p|} \quad (19)$$

where the drag coefficient, C_d , is taken to be the following:

$$C_d = \left(\frac{24}{Re_p}\right)\left(1 + 0.15Re_p^{0.687}\right) \quad (20)$$

with the particle Reynolds number, Re_p , defined as

$$Re_p = \frac{|\bar{\mathbf{u}}(x_p)-\mathbf{u}_p|d_p}{\nu} \quad (21)$$

The drag law (Eq. (20)) used in the current work is valid for $Re_p < 800$ [22]. The particle equation of motion is solved using the fourth-order Runge–Kutta scheme. The dimensionless particle response time (Stokes number) can be defined either as $\tilde{\tau}_p = \tau_p(u_r/\delta)$ or as $\tau_p^+ = \tilde{\tau}_p Re_\tau$ in wall units. In this study, we have performed computations for 10 different Stokes numbers, given in Table 1 along with corresponding particle diameters and density ratios. In the context of LES with small particles, one needs to also consider the particle motion due to the subgrid scale turbulence. The effects of the subgrid scales are more important to the transport of low τ_p^+ particles rather than the high τ_p^+ ones [7]. However, there is no unique way of including the effects of unresolved fluid flow scales on particle motion. In the context of the kinetic energy based subgrid scale models, it is possible to evaluate a velocity scale as $\sqrt{2k_{sgs}/3}$. This representative velocity can be added isotropically to the resolved fluid velocity with an imposed Gaussian distributed random number (of zero mean). This practice is consistent with the formulation of the isotropic eddy viscosity and the assumed universality of the small scales.

The particles are initially positioned randomly in the domain with initial velocities equal to the local fluid velocity. The particles are advanced from these positions and are assumed to deposit when they are within a distance of one radius from the wall. Statistics of the deposition patterns are then computed.

2.4. Particle collisions

Particle collisions are naturally important in flows with large particle volume fractions ($>10^{-3}$), but can also be important in certain local regions of a dilute gas particle flow. In this study, we have also considered the effects of inter-particle collisions on the deposition rates and patterns. There are two basic approaches to detect collisions between particles. The simplest is to use a purely retroactive method [18,23,24]. It is the cheapest from a computational viewpoint. However, the retroactive method can underestimate the number of collisions. A fully proactive method [18] captures (from a geometric standpoint) all collisions, but is computationally expensive since the collision algorithm is an $O(N^2)$ operation, where N is the number of particles in the domain. An approach that is more accurate than the purely retroactive method, but computationally less intensive than the proactive method, has been previously developed [25] (by the current authors) and used in this work. This method is briefly described below.

The flow domain is first partitioned into sections in which collisions will be considered. In this work, $16 \times 16 \times 16$ uniform partitions are used. It is assumed that the particles have constant velocities during a time step. Then, tracking inter-particle collisions becomes a purely geometric consideration once the initial particle positions and velocities are known. In a given partition, all collision pairs are first identified using a method similar to that of Chen et al. [24]. Next, the pairs are ordered in the ascending order of their time for collision. The first collision in the ordered list (say, between particles p and q) for the partition is carried out by advancing the particles p and q to the point of impact by using the known velocities at the n th time step. Perfectly elastic collisions are assumed to compute post-collision particle velocities. Li et al. [29] have shown in a channel flow that for particle parameters similar to those in the

Table 1
Overview of simulations

Simulation no.	ρ_p/ρ_f	d_p/δ	d^+	$\tau_p/(\delta/u_r)$	τ_p^+	ϕ_v	Coupling type
1	1000	0.0001	0.036	0.0002	0.072	8.33×10^{-9}	One-way
2	1000	0.00025	0.09	0.0013	0.45	1.30×10^{-7}	One-way
3	1000	0.0005	0.18	0.005	1.8	1.04×10^{-6}	One-way
4	1000	0.001	0.36	0.02	7.2	8.33×10^{-6}	One-way
5	1000	0.002	0.72	0.08	28.8	6.67×10^{-5}	One-way
6	8900	0.0001	0.036	0.0018	0.6408	8.33×10^{-9}	One-way
7	8900	0.00025	0.09	0.0111	4.005	1.30×10^{-7}	One-way
8	8900	0.0005	0.18	0.0445	16.02	1.04×10^{-6}	One-way
9	8900	0.001	0.36	0.178	64.08	8.33×10^{-6}	One-way
10	8900	0.002	0.72	0.712	256.32	6.67×10^{-5}	One-way
11	1000	0.0005	0.18	0.005	1.8	1.04×10^{-6}	Four-way
12	1000	0.002	0.72	0.08	28.8	6.67×10^{-5}	Four-way
13	8900	0.002	0.72	0.712	256.32	6.67×10^{-5}	Four-way
14	8900	0.002	0.72	0.712	256.32	10^{-3}	Two-way
15	8900	0.002	0.72	0.712	256.32	10^{-3}	Four-way

present study, the results remain virtually unchanged even when a 10% energy loss is considered during the collisions. The collision list is then modified such that any future collision that contains particles p and q is not allowed to occur in the same time step. Subsequently, the pair next in the list to p and q is made to collide and is then removed from future collisions during the current time step. This process is repeated until there are no more particles left in the collision list. The inclusion of this collision algorithm required approximately three times more CPU time for a given simulation compared to that without collisions. Further details of the algorithm are presented in Rani et al. [25].

3. Results

A parametric study of the effects of varying particle relaxation time, τ_p^+ , on wall-deposition has been performed. In addition to the one-way coupled simulations, the effects of two-way coupling (inclusion of particle feedback effects) and four-way coupling (two-way with particle collisions) on deposition have been investigated. The various parameters considered are given in Table 1. To give a perspective on typical dimensional values of these parameters, if the duct cross-section is $1\text{ m} \times 1\text{ m}$, the particle sizes will vary from $100\text{ }\mu\text{m}$ to 2.0 mm . The bulk flow velocity for air in the duct would be roughly 0.1 m/s .

The fluid statistics are averaged in time for more than 60 dimensionless time units (δ/u_τ). These results were compared to the DNS data of Gavrilakis [15], who studied the flow at $Re_\tau=300$. Good agreement is seen in the mean streamwise velocity, which is shown in Winkler et al. [1] The v_{rms} obtained by the present work deviates not more than 15% from the DNS done by Gavrilakis [15], with the other rms velocities comparing even better [1]. Contours of the streamwise velocity, shown in Fig. 3, also agree with previous studies [15,27]. The smooth and symmetric nature of these velocity contours indicates that the

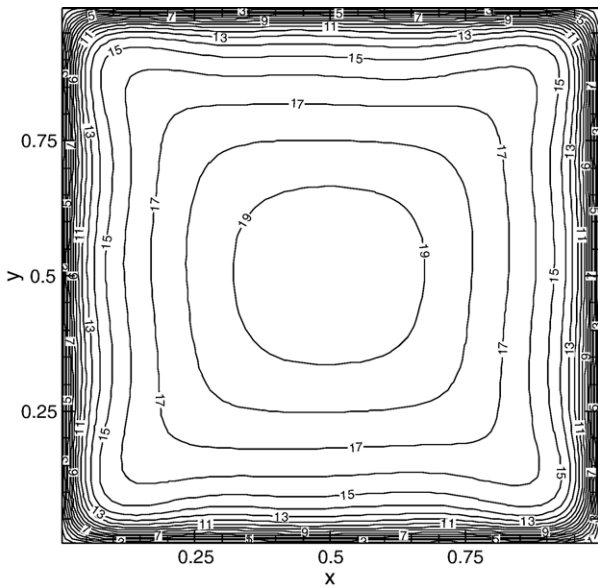


Fig. 3. Mean streamwise velocity contours.

fluid turbulence has indeed been evolved to a statistically stationary state.

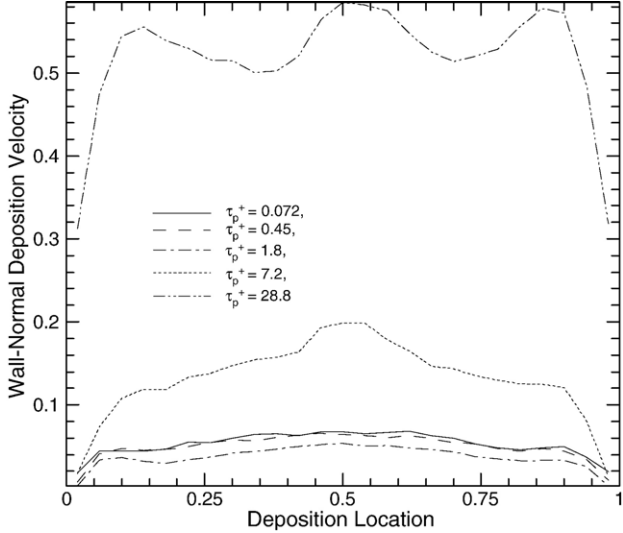
We have considered particle volume fractions as high as 10^{-3} to study the effects of two-way coupling and particle collisions on deposition. We present the probability distribution functions (PDFs) of (i) particle deposition locations, (ii) the average streamwise and wall-normal deposition velocities, and (iii) the deposition rates, to quantify particle deposition patterns. The deposition statistics are averaged for 34 time units in the case of particles with $\tau_p^+=0.072$ ($\tilde{\tau}_p=0.0002$) and 8 time units in the case of particles of $\tau_p^+=256.32$ ($\tilde{\tau}_p=0.712$). These averaging times correspond to 1.7×10^5 and 11 response times for the least and the most inertial particles, respectively. In addition, due to the homogeneous streamwise direction, and the $\pi/2$ rotation symmetry about the duct axis, the statistics are averaged over the four duct walls. Due to the higher deposition rates of the large τ_p^+ particles, lesser averaging time was needed to obtain deposition statistics. We will first present the results with one-way coupling, followed by a discussion of the effects of two-way and four-way coupling.

3.1. One-way coupling

3.1.1. Wall-normal deposition velocity

The deposition velocities in the wall-normal and the streamwise directions are of interest in studying the erosion of the duct walls. In a channel or a pipe flow, the time-averaged deposition velocity is uniform over the wall due to the two homogeneous directions parallel to the wall. However, in a square duct, due to the inhomogeneous nature of the flow in the cross-sectional plane, the deposition velocities vary along the duct walls, but have a 90° rotational symmetry about the duct axis. In this section we present the particle deposition velocities as a function of dimensionless particle response time, τ_p^+ . Two-way and four-way coupling effects are not considered. Results have been presented for 10 different values of τ_p^+ , corresponding to two values of particle/fluid density ratio ($\rho_p/\rho_f=1000$ and 8900) and five particle diameters for each density ratio. The various parameters considered in this section correspond to simulations 1–10 in Table 1. The two values of ρ_p/ρ_f chosen correspond to water/air and copper/air flows for which experiments can be readily conducted in future.

Fig. 4 presents the wall-normal deposition velocities, as a function of the deposition location, for five τ_p^+ values corresponding to $\rho_p/\rho_f=1000$. Here, we see several interesting trends. First, as the value of τ_p^+ is increased from 0.072 to 1.8, the wall normal deposition velocity does not change appreciably. However, further increase in τ_p^+ from 1.8 to 28.8 leads to a substantial increase in the wall-normal deposition velocity across the duct width. Also, we clearly see that the deposition velocity varies along the duct walls. The deposition velocity is lowest at the corners of the duct (deposition locations, $x, y=0$ and 1), and then increases progressively as we move away from the corners. Because of the rotational symmetry, the horizontal axis in Fig. 4 corresponds to either x or y . For $\tau_p^+=28.8$, we also see secondary peaks in the deposition velocity at roughly 15% of the duct width from the corners. For all the particle response

Fig. 4. Wall-normal deposition velocity, $\rho_p/\rho_f=1000$, one-way coupling.

times considered, the maximum deposition velocity occurs at the center of the duct wall. We believe this is due to the relatively large streamwise velocity gradients in the wall-normal direction at this location compared to the corners (as is shown in Fig. 5). The larger stream-wise velocity gradients cause a larger lift force (directed towards the wall) and thus, an increased wall-normal deposition velocity. Note that Fig. 5 is the fluid velocity for the one-way coupled simulations.

The wavy nature of the wall-normal deposition velocities can be explained by examining the wall-normal gradients of the mean streamwise velocity at the duct wall, shown in Fig. 5. This figure shows a wavy pattern that is qualitatively similar to the mean wall shear stress pattern shown in Gavrilakis [15]. The wall shear stress, τ_{wall} , is proportional to the wall-normal gradients of the streamwise velocity, and thus, locally high values of wall shear stress will indicate locations where the lift force is large.

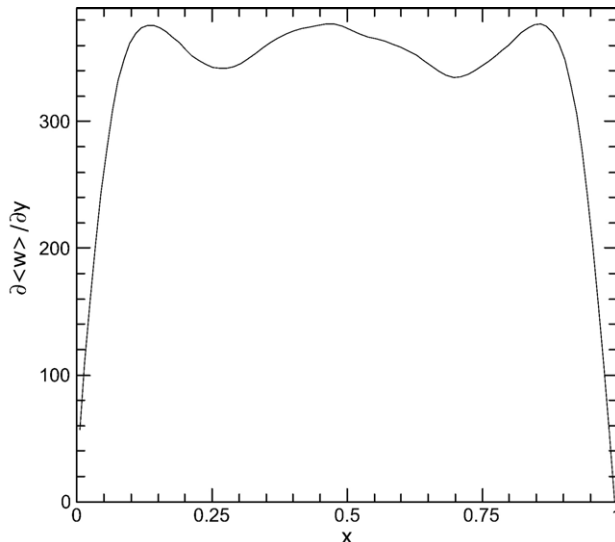
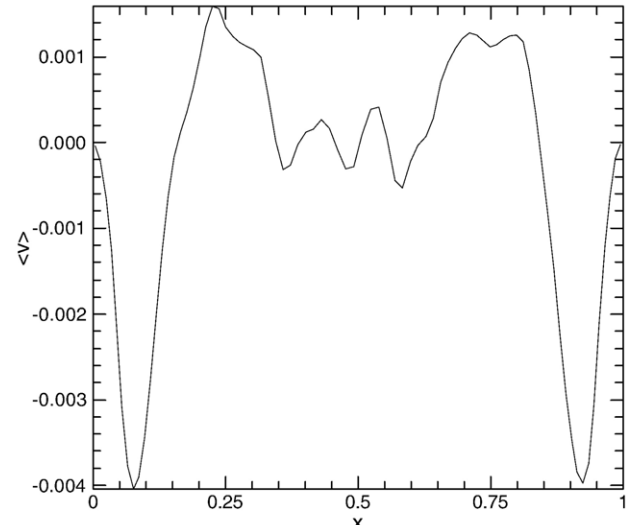
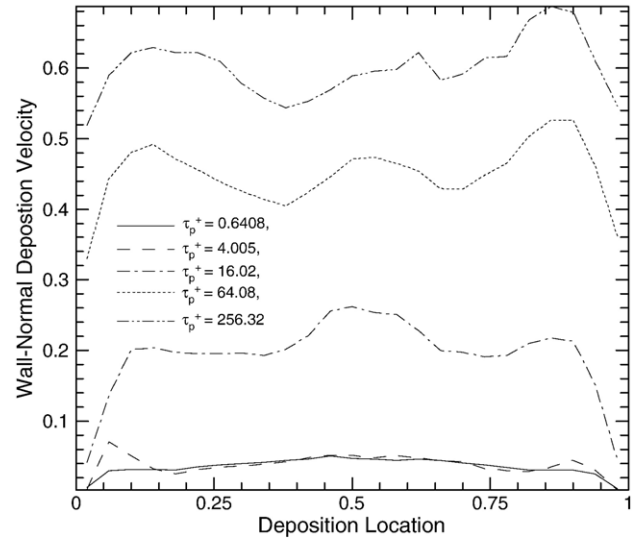


Fig. 5. Variation of wall streamwise velocity gradient.

Fig. 6. Average wall-normal fluid velocity at $y^+=1.76$.

The wall-normal component, $\langle v \rangle$, of the mean fluid velocity near the wall (shown in Fig. 6) also supports the wavy deposition pattern. In Fig. 6, the locations where $\langle v \rangle$ is negative, i.e. where the mean flow is towards the wall, corresponds approximately to the locations where we see secondary peaks in $\langle v_p \rangle$, i.e. the wall-normal deposition velocity of the particles. Hence, we can say that this mean fluid flow towards the wall also contributes to the secondary peaks seen in Fig. 4.

The wall-normal deposition velocities for the τ_p^+ corresponding to $\rho_p/\rho_f=8900$ are shown in Fig. 7. The wall-normal deposition velocity is seen to increase with τ_p^+ for the range of response times examined, except for the smallest values of τ_p^+ . The non-uniform velocity profile across the duct width is more apparent here, compared to the cases with the lower density ratio.

Fig. 7. Wall-normal deposition velocity, $\rho_p/\rho_f=8900$, one-way coupling.

3.1.2. Streamwise deposition velocity

The streamwise deposition velocity is a good measure of the slip between the particles and the fluid in the near wall region since the fluid velocity goes to zero at the walls. We can see in Fig. 8 that the less inertial particles (smaller τ_p^+) deposit on the wall with lower streamwise velocities. This is because as the particles approach the wall, those with lower inertia respond better to fluid deceleration than those with higher inertia. In Fig. 8, we see that the $\tau_p^+ = 28.8$ particles noticeably retain streamwise momentum even after passing through the near-wall shear layer. In fact, these particles have significant velocities even near the corners of the walls. Further, the wavy pattern of the velocity profile for the $\tau_p^+ = 28.8$ particles demonstrates the effects of secondary mean flows. The fluid mean streamwise velocity profile at $y^+ = 1.76$, shown in Fig. 9, also displays a similar wavy pattern across the duct width. As a result, the deposition velocity is seen to exhibit a wavy pattern with a maximum at the center of the duct wall (where the fluid mean streamwise velocity is maximum for a given y^+), and two secondary peaks. For density ratio $\rho_p/\rho_f = 8900$, we see the above trends in a more pronounced fashion (shown in Fig. 10). In Fig. 10, as τ_p^+ is increased to 256.32, we see a progressive increase in the streamwise deposition velocities. This is because as τ_p^+ increases, particles are less responsive to the surrounding fluid and hence, retain their momentum even after passing through the fluid boundary layer near the wall.

3.1.3. Deposition location

In pipe and channel flows, the directions parallel to the walls are both homogeneous and hence, the mean profile of the number of deposited particles does not vary along the walls. For a square duct, however, the deposition pattern is more complex because of the inhomogeneity of the directions parallel to the walls (except the streamwise direction). Shown in Fig. 11 are the PDFs of the deposition location for particles corresponding

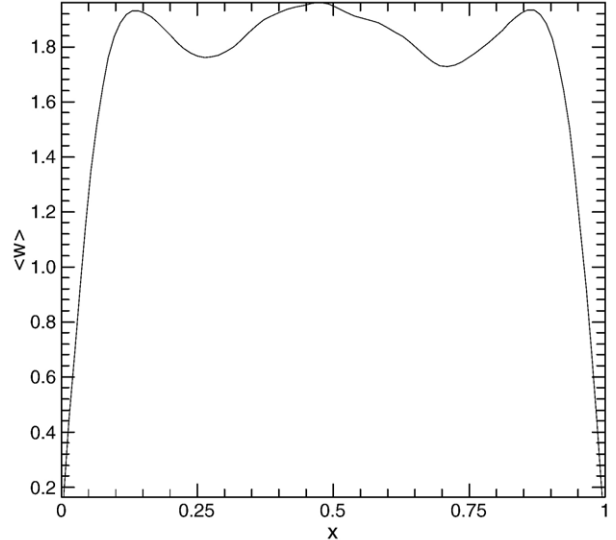


Fig. 9. Average streamwise velocity at $y^+ = 1.76$.

to $\rho_p/\rho_f = 1000$. Here, we can identify several trends. First, for all the particle relaxation times examined, deposition is more probable near the center of the duct wall than near the corners. In fact, for particles with $\tau_p^+ = 0.072$ and 0.45, we see only a very small fraction of particles depositing near the duct corners. These trends in the deposition location are supported by the wall-normal deposition velocity profiles as well (see Figs. 4 and 7). The maximum wall-normal deposition velocity occurs near the duct center leading to greater deposition here and the minimum occurs near the corners. As τ_p^+ is increased, the PDF profiles are flattened, i.e. the particles tend to deposit more uniformly across the duct width. Deposition near the corners also increases. For $\rho_p/\rho_f = 8900$, the PDFs of the deposition location show similar trends (Fig. 12). The increasing uniformity in particle deposition

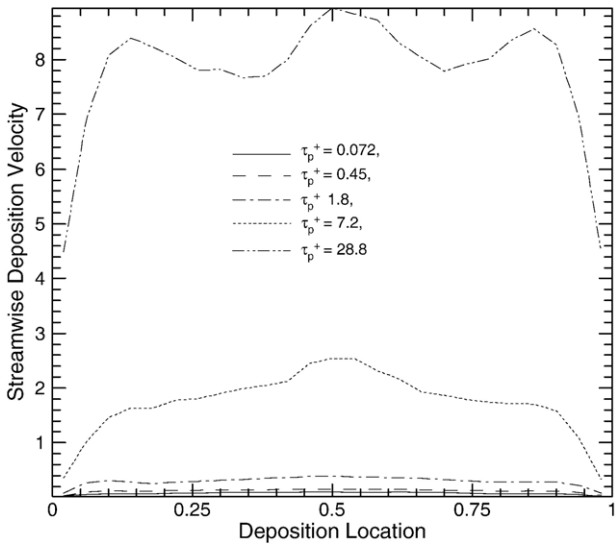


Fig. 8. Streamwise deposition velocity, $\rho_p/\rho_f = 1000$, one-way coupling.

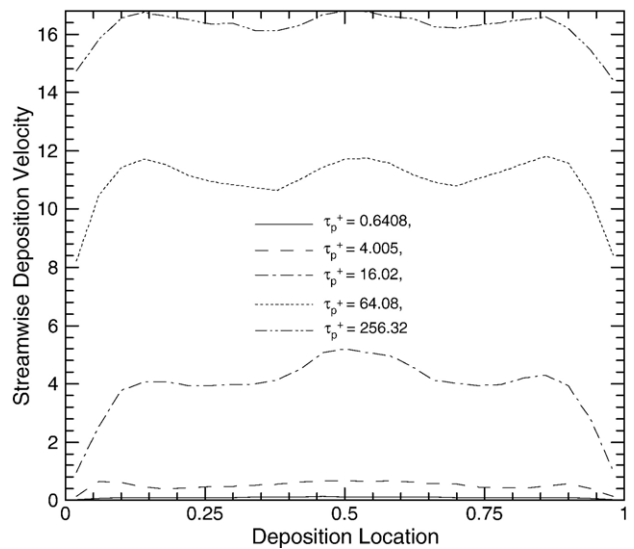
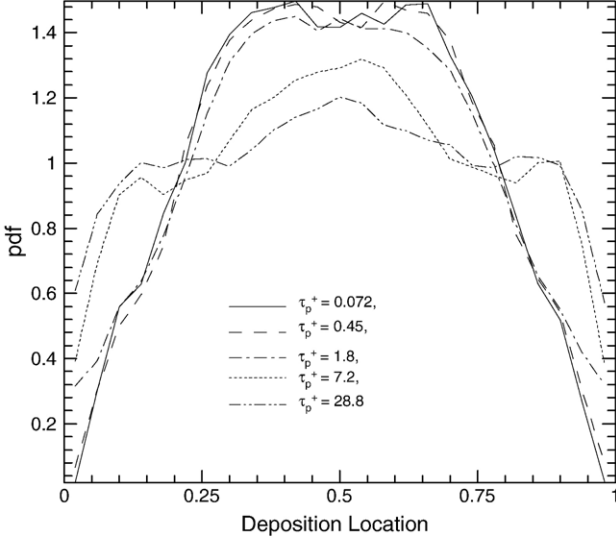


Fig. 10. Streamwise deposition velocity, $\rho_p/\rho_f = 8900$, one-way coupling.

Fig. 11. PDFs of deposition location, $\rho_p/\rho_f=1000$, one-way coupling.

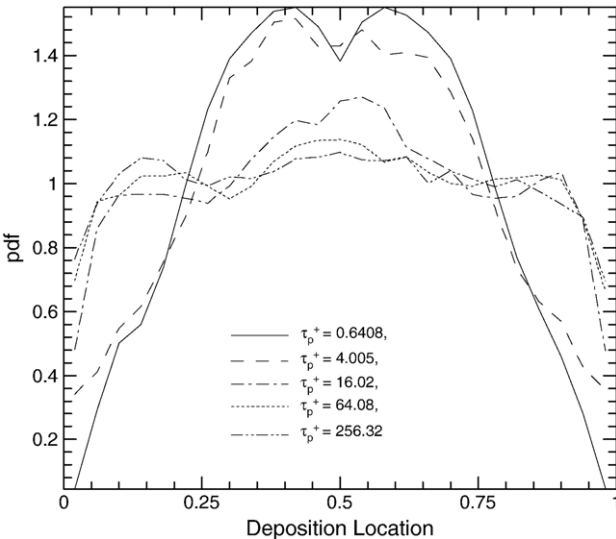
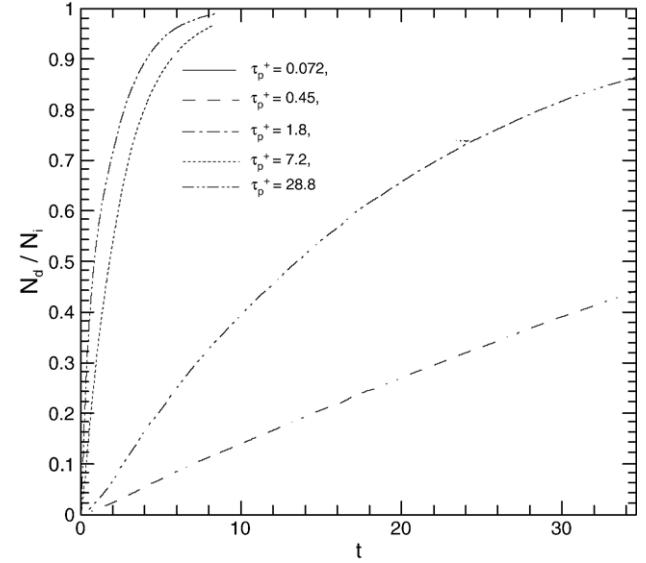
across the duct width with particle response time can be more clearly observed in Fig. 12.

3.1.4. Deposition rates

Deposition rates are important in studying phenomena such as droplet impingement on a heat exchanger surface, dust deposition on surfaces in clean rooms, etc. An average particle deposition rate, V_d , can be estimated as follows [7]:

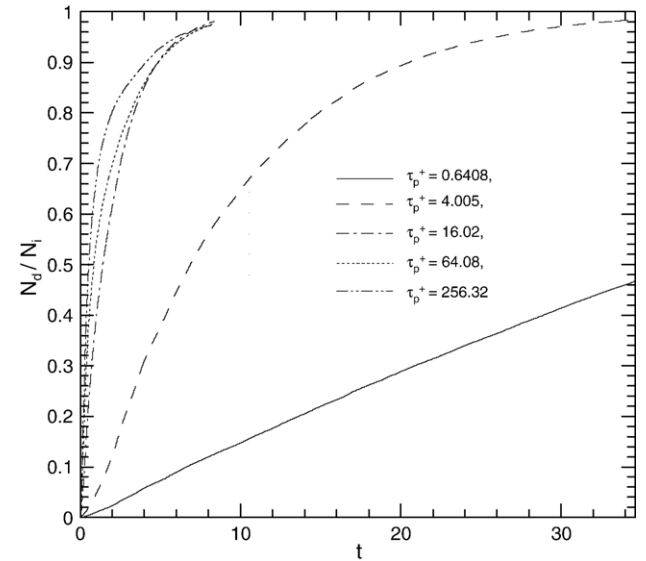
$$V_d = \frac{N_d/A/t}{N/V} \quad (22)$$

where N_d is the number of deposited particles during a time period t , A is the area of deposition, N is the number of particles in the entire domain at the beginning of the deposition sampling time, and V is the volume of the domain. The time period used

Fig. 12. PDFs of deposition location, $\rho_p/\rho_f=8900$, one-way coupling.Fig. 13. Time history of particle deposition, $\rho_p/\rho_f=1000$, one-way coupling.

to calculate the deposition rate was such that the number of deposited particles per unit time reaches a quasi-equilibrium state [8]. In Figs. 13 and 14, we plot the number of deposited particles, N_d , normalized by the number of initial particles, N_i , as a function of time for $\rho_p/\rho_f=1000$ and 8900, respectively. It is clear that the particles with higher inertia deposit faster than those with lower inertia. This trend agrees with previous studies in pipe and channel flows [7,28].

In Fig. 15, we plot the deposition rates normalized by the average friction velocity and compare them with the empirical correlations developed for a pipe flow by McCoy and Hanratty [28] and Liu and Agarwal [26]. The trends are similar to those seen in pipe flow. However, for small particles, the deposition rates in a square duct are higher than those in a pipe flow. It is interesting to note that for high inertia particles, the correlation

Fig. 14. Time history of particle deposition, $\rho_p/\rho_f=8900$, one-way coupling.

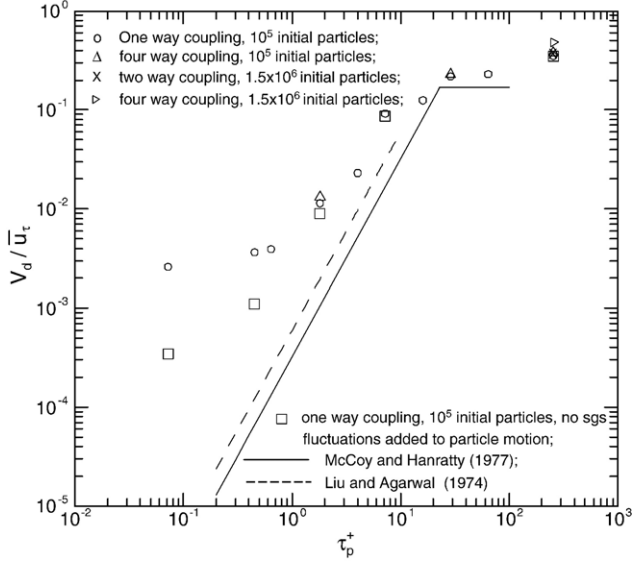


Fig. 15. Deposition rates compared with experimental pipe flow data.

of McCoy and Hanratty [28] agrees well with the square duct deposition rates. This may be because the largest particles are not as sensitive to the secondary mean flows that are absent in a pipe flow and thus more closely match pipe flow results.

To study the effects of the subgrid fluctuations on particle deposition rates, one-way coupling simulations with five particle response times, in which the subgrid fluctuations are not included in the particle evolution, were performed. The results are also shown in Fig. 15. It is observed that when sgs fluctuation effects are neglected, the deposition rate is reduced for low inertia particles ($\tau_p^+ < 2$), but remains nearly the same for the more inertial particles. This is to be anticipated since the high inertia particles will be less responsive to the subgrid fluctuations than the low inertia ones. This result is similar to that obtained by Wang and Squires [7] who state that for $\tau_p^+ > 6$ particles, there is almost no difference in the results obtained with and without the subgrid contribution.

Next, we study the effects of including the two-way and four-way coupling effects on particle deposition patterns. In two-way coupling, only the effects of particles on the fluid are considered, while in four-way coupling particle-particle collisions are considered as well.

3.2. Effects of two-way and four-way coupling

3.2.1. Low volume fraction ($\phi_v \leq 10^{-4}$)

At particle volume fractions $\phi_v \leq 10^{-4}$, it is expected that neither particle feedback effects nor collisions will play a major role. However, locally high particle volume fractions due to the preferential concentration of particles may warrant the inclusion of the above effects. Hence, to begin with, we examine the effects of four-way coupling at low volume fractions for three representative particle response times ($\tau_p^+ = 1.8$, 28.8, and 256.32). The effects of two-way and four-way coupling depend on particle concentration, which in turn is a function of time as particles deposit on the surface. The results shown in this section are representative of an experiment where the particles in the domain are allowed to deposit until no particles remain in

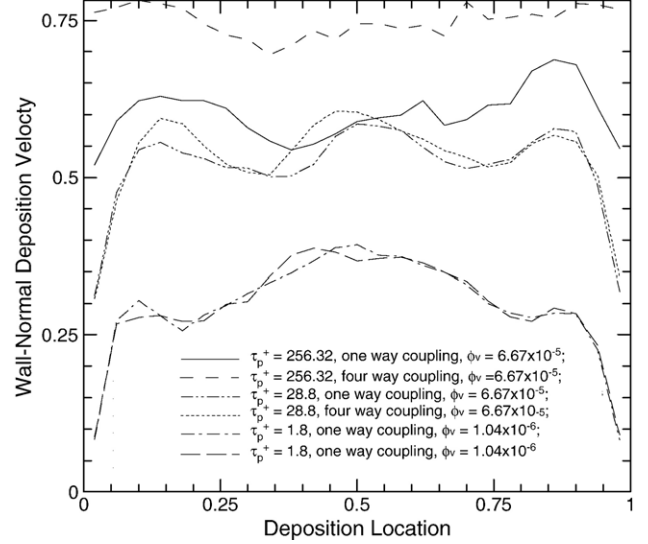


Fig. 16. Wall-normal deposition velocity, four-way coupling, 10^5 initial particles.

the flow field. It would be computationally much more expensive to hold the number of particles in the flow domain constant, as each new particle introduced for every deposited particle would have to be allowed to adjust to the flow and lose its initial transients.

By examining the wall-normal deposition velocity, shown in Fig. 16, we see that four-way coupling does not appreciably change the deposition velocities for $\tau_p^+ = 1.8$. This is reasonable since the volume fraction for this response time is very low ($\phi_v = 1.4 \times 10^{-6}$). For particles with $\tau_p^+ = 28.8$ ($\phi_v = 6.67 \times 10^{-5}$) as well, we see only a small difference in the wall-normal deposition velocities for the one-way and four-way cases. However, for the $\tau_p^+ = 256.32$ particles, we see a significant increase in the wall-normal deposition velocity when four-way coupling is considered. As will be shown later, this effect can be largely attributed to the inclusion of particle collisions.

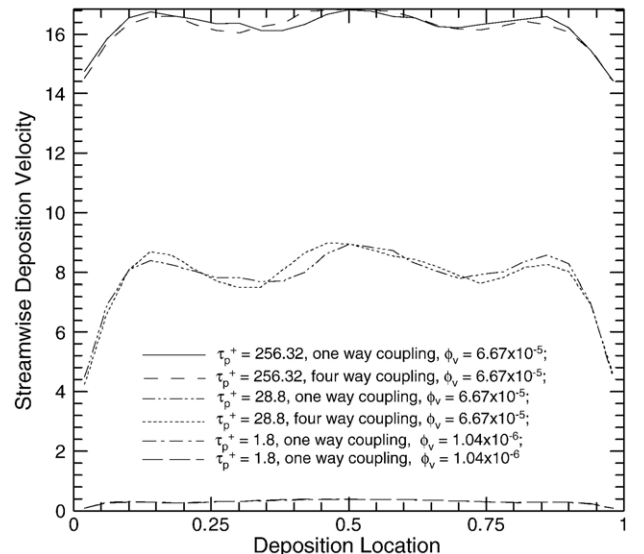


Fig. 17. Streamwise deposition velocity, four-way coupling, 10^5 initial particles.

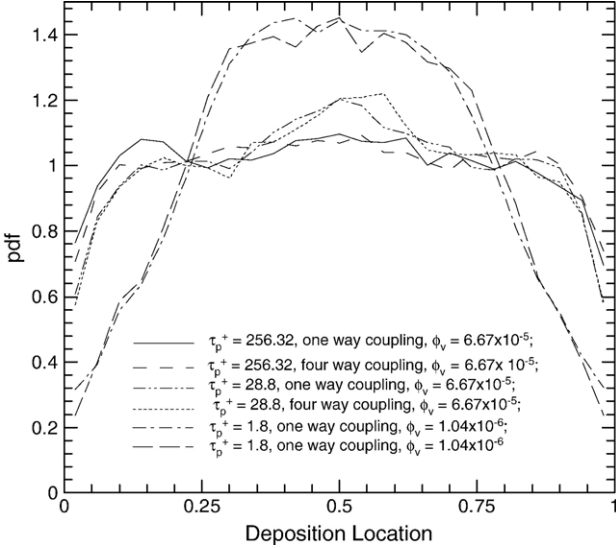


Fig. 18. PDFs of deposition location, four-way coupling, 10^5 initial particles.

The streamwise deposition velocities for both one-way and four-way coupled cases are shown in Fig. 17. No significant difference was observed even at the highest response time.

In Fig. 18, we examine the effects of four-way coupling on the deposition location for $\phi_v \leq 6.67 \times 10^{-5}$. No appreciable differences can be seen for any of the Stokes numbers examined. This indicates that neither collisions nor particle feedback significantly alter the deposition location of particles for volume fractions of the order of 6.67×10^{-5} or less.

In Fig. 19, the number of deposited particles (normalized by the number of initial particles) as a function of time is shown for the six cases (three values of τ_p^+ and two values of ϕ_v). In all these cases (with $\phi_v \leq 6.67 \times 10^{-5}$), four-way coupling increased the deposition rates. The deposition rates calculated from Fig. 15 are also included in Fig. 15 and show similar trends

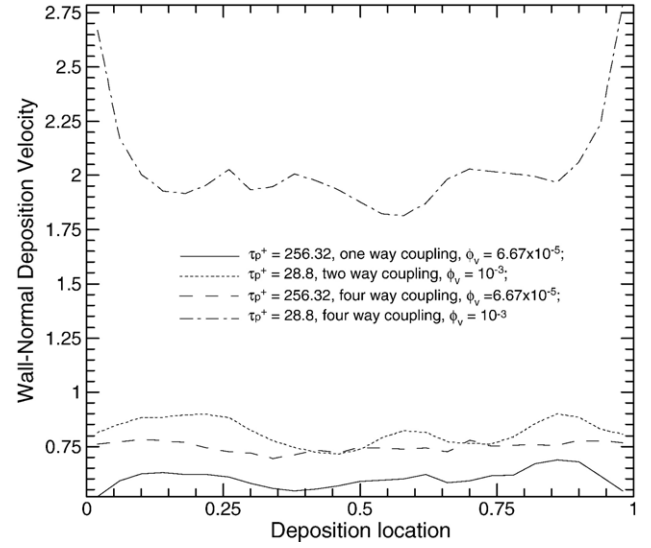


Fig. 20. Wall-normal deposition velocity, two-way and four-way coupling, volume fraction = 10^{-3} .

as the corresponding one-way cases. Although the differences between one-way and four-way coupled results are not large, the trend of increased deposition rates as a result of four-way coupling is apparent. However, due to the relatively small differences in the results for one-way and four-way coupled cases (for most statistics examined), we feel that the one-way coupling approach is sufficiently accurate for computing gas-particle flows with volume fractions less than 6.67×10^{-5} .

3.2.2. Higher volume fraction ($\phi_v = 10^{-3}$)

To further understand the effects of two-way coupling and particle collisions, we increase the volume fraction to a level where they are likely to be significant. Therefore, one set of simulations with both two-way and four-way coupling was performed for $\tau_p^+ = 256.32$ with an initial volume fraction of

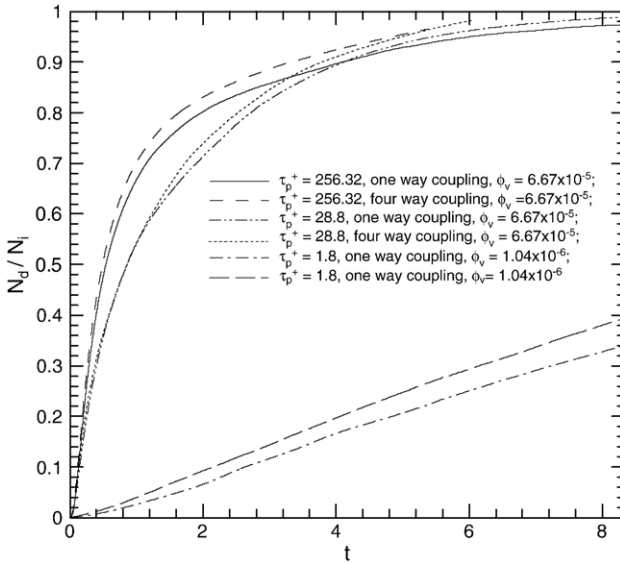


Fig. 19. Time history of particle deposition, four-way coupling, 10^5 initial particles.

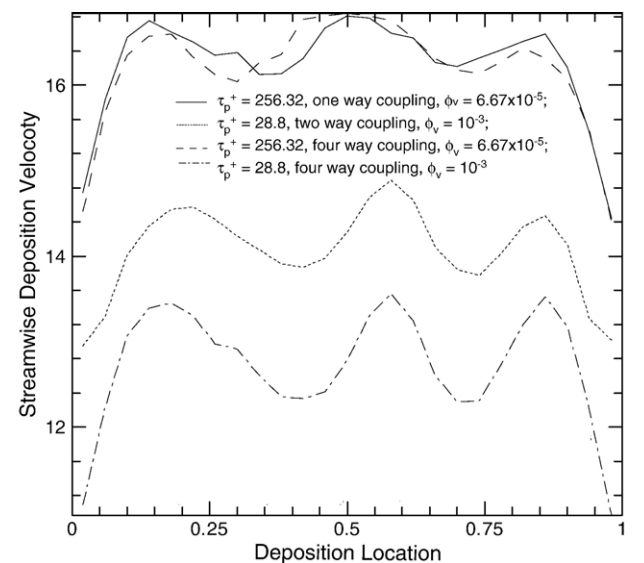


Fig. 21. Streamwise deposition velocity, two-way and four-way coupling, volume fraction = 10^{-3} .

10^{-3} , which corresponds to 1.5 million initial particles in the domain. These simulations will help us isolate the effects of two-way coupling and the particle–particle collisions.

The wall-normal deposition velocity is shown in Fig. 20. Previous one-way and four-way coupled results with 100,000 initial particles ($\phi_v=6.67 \times 10^{-5}$) are also included for comparison. At $\phi_v=10^{-3}$ with only two-way coupling, we see slightly higher wall-normal deposition velocities when compared to those at $\phi_v=6.67 \times 10^{-5}$. This indicates that the particle feedback effect leads to a marginal increase in wall-normal deposition velocities. However, when four-way coupling at $\phi_v=10^{-3}$ is included, we see appreciable differences in the results. It is observed that the maximum wall-normal deposition velocity now occurs near the corners. Compared to the results at lower volume fractions in Section 3.2.1, there is a distinct flattening of the profile, i.e. the secondary peaks become less prominent and the maximum now occurs at the corners. This suggests a lateral transfer (i.e. parallel to the wall) of momentum between the particles due to collisions at high volume fractions. The deposition velocity is increased by a factor of more than two due to collisions. This clearly indicates that the inclusion of particle–particle collisions can significantly alter the results of wall-normal deposition velocities at relatively high volume fractions.

The streamwise particle deposition velocities for $\tau_p^+=256.32$ are shown in Fig. 21. With two-way coupling, the increase in volume fraction is clearly seen to decrease the streamwise deposition velocities. Inclusion of particle collisions, i.e. four-way coupling, is seen to decrease the deposition velocities even further than the two-way case at $\phi_v=10^{-3}$. Higher volume fractions are also seen to increase the non-uniformity across the duct walls for the streamwise deposition velocities.

The PDFs of the deposition location are shown in Fig. 22. Two-way coupling is seen to marginally augment the non-uniform deposition pattern, when compared to the one-way coupled results at $\phi_v=6.67 \times 10^{-5}$. The effects of collisions on

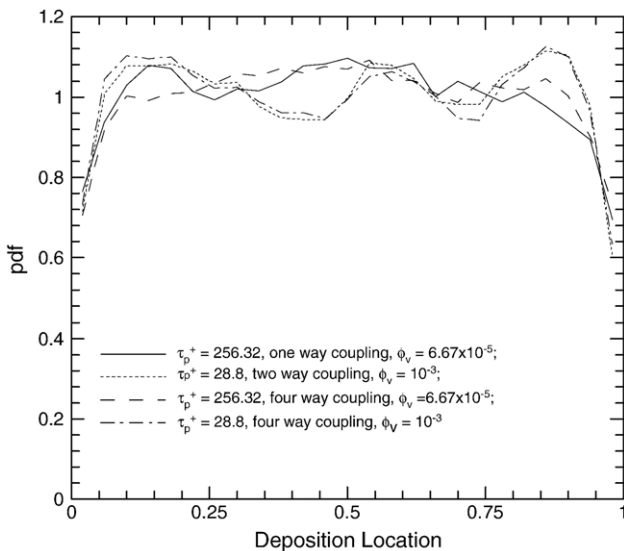


Fig. 22. PDFs of deposition location, two-way and four-way coupling, volume fraction= 10^{-3} .

deposition location, which can be observed by comparing the two-way and four-way coupling results, are not significant even at $\phi_v=10^{-3}$. We can thus conclude that collisions do not alter the deposition location significantly even at high volume fractions.

The deposition rates, normalized by the average friction velocity, for $\phi_v=10^{-3}$ have been included in Fig. 15 itself (denoted as the case with 1.5×10^6 particles), along with the earlier lower volume fraction results. It is seen that both two-way and four-way couplings increase deposition rates. Thus, the effect of collisions on increasing the deposition rate is again apparent.

4. Conclusions

The deposition of particles in a fully developed turbulent square duct flow was studied using large eddy simulations. Ten particle Stokes numbers, corresponding to two density ratios ($\rho_p/\rho_f=1000$ and 8900) and five particle diameters ($d_p/\delta \times 10^6=100$, 250 , 500 , 1000 and 2000), were studied. Two particle number densities corresponding to initial particle numbers of 10^5 and 1.5×10^6 were examined. In addition to one-way coupling, two-way, and four-way coupling effects were also considered.

In general, the wall-normal deposition velocity is seen to increase with Stokes number. For one-way coupling, the maximum wall-normal deposition velocity occurs near the center of the duct wall. However, collisions cause this maximum to occur near the corners. The streamwise deposition velocity is seen to increase with the particle response time. Secondary mean flows are found to cause a wavy pattern in the deposition velocity profile across the duct width. The streamwise deposition velocity is seen to be highest near the center of the duct wall for all particle response times examined. Two-way coupling and collision effects decrease the streamwise deposition velocity.

Deposition is seen to be least likely in the duct corners, and most likely in the duct center. As the Stokes number is increased, the deposition pattern becomes more uniform across the duct width. Two-way coupling effects tend to cause an augmentation of the wavy deposition pattern. At low volume fractions, inclusion of two-way coupling and particle collisions did not significantly alter the deposition trends. As a result, the one-way coupled approach is sufficient for volume fractions less than 10^{-4} .

Deposition rates are computed and compared to experimental data in pipes and ducts. The present results agree qualitatively with results in pipe flows. However, for small particles, the deposition rate in the square duct is two orders of magnitude higher than in a pipe. For large particles, the deposition rates in a square duct are closer to those in a circular pipe. Lastly, two-way and four-way couplings are seen to enhance the deposition rates.

Acknowledgements

The financial supports of the Air Conditioning and Refrigeration Center at the University of Illinois at Urbana-Champaign and the Center for Simulation of Advanced Rockets

at the University of Illinois, which is funded by the US Department of Energy through the University of California under Subcontract number B341494, are gratefully acknowledged.

References

- [1] C.M. Winkler, S.L. Rani, S.P. Vanka, Preferential concentration of particles in a fully developed turbulent square duct flow, *Int. J. Multiph. Flow* 30 (1) (2004) 27–50.
- [2] J.R. Fessler, J.D. Kulick, J.K. Eaton, Preferential concentration of heavy particles in a turbulent channel flow, *Phys. Fluids* 6 (11) (1994) 3742.
- [3] K.D. Squires, J.K. Eaton, Preferential concentration of particles by turbulence, *Phys. Fluids* 3 (5) (1991) 1169.
- [4] J. Ferry, S. Balachandar, A fast Eulerian method for disperse two-phase flow, *Int. J. Multiph. Flow* 27 (2001) 1199.
- [5] E. Loth, Numerical approaches for motion of dispersed particles, droplets and bubbles, *Prog. Energy Combust. Sci.* 26 (2000) 161.
- [6] C. Meneveau, J. Katz, Scale-invariance and turbulence models for large eddy simulation, *Annu. Rev. Fluid Mech.* 32 (2000) 1.
- [7] Q. Wang, K.D. Squires, Large eddy simulation of particle deposition in a vertical turbulent channel flow, *Int. J. Multiph. Flow* 22 (4) (1996) 667.
- [8] H. Zhang, G. Ahmadi, Aerosol particle transport and deposition in vertical and horizontal turbulent duct flow, *J. Fluid Mech.* 406 (2000) 55.
- [9] W.S.J. Uijttewaal, R.V.A. Oliemans, Particle dispersion and deposition in direct numerical and large eddy simulations of vertical pipe flows, *Phys. Fluids* 8 (10) (1996) 2590.
- [10] J.W. Brooke, T.J. Hanratty, J.B. McLaughlin, Free-flight mixing and deposition of aerosols, *Phys. Fluids* 8 (10) (1994) 3404.
- [11] B. van Haarlem, B.J. Boersma, F.T.M. Nieuwstadt, Direct numerical simulation of particle deposition onto a free-slip and no-slip surface, *Phys. Fluids* 10 (10) (1998) 2608.
- [12] R.K. Madabhushi, S.P. Vanka, Large eddy simulation of turbulence-driven secondary flow in a square duct, *Phys. Fluids* 3 (11) (1991) 2734.
- [13] A.O. Demuren, W. Rodi, Calculation of turbulence-driven secondary motion in non-circular ducts, *J. Fluid Mech.* 140 (1984) 189.
- [14] T. Kajishima, Y. Miyake, A discussion on eddy viscosity models on the basis of the large eddy simulation of turbulent flow in a square duct, *Comput. Fluids* 21 (2) (1992) 151.
- [15] S. Gavrilakis, Numerical simulation of low-Reynolds-number turbulent flow through a straight square duct, *J. Fluid Mech.* 244 (1992) 101.
- [16] A. Huser, S. Biringen, Direct numerical simulation of turbulent flow in a square duct, *J. Fluid Mech.* 257 (1993) 65.
- [17] R.K. Madabhushi, S.P. Vanka, Direct numerical simulations of turbulent flow in a square duct at low Reynolds number, in: R.M.C. So, C.G. Speziale, B.E. Launder (Eds.), *Near-Wall Turbulent Flows*, Elsevier, 1993, p. 297.
- [18] S. Sundaram, L.R. Collins, Numerical considerations in simulating a turbulent suspension of finite-volume particles, *J. Comput. Phys.* 124 (2) (1996) 337.
- [19] W.W. Kim, S. Menon, Application of the localized dynamic subgrid-scale model to turbulent wall-bounded flows, *AIAA 97-0210*, 1997.
- [20] D.K. Lilly, A proposed modification of the Germano Subgrid-scale Closure Model, *Phys. Fluids* 4 (3) (1992) 633.
- [21] C.M. Winkler, S.L. Rani, Forces on particles in a turbulent square duct flow, *American Physical Society 56th Annual Meeting of the Division of Fluid Dynamics*, Session JG, Multiphase Flows IV, New Jersey, 2003.
- [22] M. Boivin, O. Simonin, K.D. Squires, Direct numerical simulation of turbulence modulation by particles in isotropic turbulence, *J. Fluid Mech.* 375 (1998) 235.
- [23] Y. Yamamoto, M. Potthoff, T. Tanaka, T. Kajishima, Y. Tsuji, Large-eddy simulation of turbulent gas-particle flow in a vertical channel: effect of considering inter-particle collisions, *J. Fluid Mech.* 442 (2001) 303.
- [24] M. Chen, K. Kontomaris, J.B. McLaughlin, Direct numerical simulation of droplet collisions in a turbulent channel flow. Part I: Collision algorithm, *Int. J. Multiph. Flow* 24 (1998) 1079.
- [25] S.L. Rani, C.M. Winkler, S.P. Vanka, A new algorithm for computing binary collisions in dispersed two-phase flows, *Numer. Heat Transf., B Fundam.* 45 (1) (2004) 99–107.
- [26] B.Y.H. Liu, J.K. Agarwal, Experimental observation of aerosol deposition in turbulent flow, *Aerosol Sci.* 5 (1974) 145.
- [27] R.K. Madabhushi, Direct and Large Eddy Simulation of Turbulent Flow in a Square Duct, Thesis, Dept. of Mech. Eng., Univ. of Illinois at Urbana-Champaign (1993).
- [28] D.D. McCoy, T.J. Hanratty, Rate of deposition of droplets in annular two-phase flow, *Int. J. Multiph. Flow* 3 (1977) 319.
- [29] Y. Li, J.B. McLaughlin, K. Kontomaris, L. Portela, Numerical simulation of particle-laden turbulent channel flow, *Phys. Fluids* 13 (10) (2001) 2957.